12-1-2006

Issues During the Inversion of Crosshole Radar Data: Can We Have Confidence in the Outcome?

William P. Clement
Boise State University

Issues During the Inversion of Crosshole Radar Data: Can We Have Confidence in the Outcome?

William P. Clement
Center for the Geophysical Investigation of the Shallow Subsurface, Boise State University, Boise, ID 83725
Fax: (208) 426-3888, Email: billc@cgiss.boisestate.edu

ABSTRACT

One method of assessing the confidence in modeled features is to compare the results from different inversion schemes. I use synthetic traveltimes calculated from a model of an unconfined aquifer to determine the reliability of crosshole tomography. I compare the inverted models from straight and curved ray approximations to wave propagation. I investigate the effects of added random noise, regularization, the starting model, and the reference model on the curved ray inversion method. I also investigate the effects of different grid sizes for the forward model and of limited ray coverage through the earth model. Understanding the effects of these different methods and parameterizations will help place confidence limits on modeled features to more accurately reflect our knowledge of the subsurface. Straight or curved ray approximations to wave propagation resulted in similar models. However, the resolution estimates are substantially different and would lead to different assessments of the model reliability. Comparisons of the different choices for the model parameterization show that the resulting models are similar, indicating that tomography is a robust method. The most important factor to obtain reliable parameter estimates from crosshole radar tomography is to acquire wide aperture, densely sampled data with little noise.

Introduction

Crosshole radar tomography is increasingly used to characterize the shallow subsurface and to monitor hydrologic processes such as infiltration through the vadose zone and solute transport through the saturated zone (Binley *et al.*, 2001; Galagedara *et al.*, 2003; Hubbard *et al.*, 2001). Typically, the surveys are conducted in wells a few meters apart and to depths of about 10 to 20 m (*e.g.*, Alumbaugh *et al.*, 2002; Binley *et al.*, 2001; Galagedara *et al.*, 2003; Tronicke *et al.*, 2002, 2004). Most of these studies report the estimated velocity models without discussing the reliability of those models. Many tomographic studies use a straight ray approximation of the ray path to linearize the problem (*e.g.*, Binley *et al.*, 2001; Galagedara *et al.*, 2003). Recently, GPR crosshole tomography studies have modeled the ray paths using curved rays (*e.g.*, Alumbaugh *et al.*, 2002; Tronicke *et al.*, 2002, 2004). Many of these studies indicate a large-scale layering in the subsurface, especially in studies imaging the saturated zone (*e.g.*, Hubbard *et al.*, 2001; Tronicke *et al.*, 2002, 2004).

Some authors have investigated the model resolution and model covariance of the tomograms for the nonlinear curved ray problem (*e.g.*, Alumbaugh and Newman, 2000; Alumbaugh *et al.*, 2002; Nolet *et al.*, 1999). However, these results are approximations to the true model resolution and model covariance matrices. The model resolution and model covariance matrices are defined for linear problems; similar model resolution or model covariance matrices are not defined for the nonlinear problem. These studies also assume that the inversion finds the global minimum and that this minimum is well-behaved so that model resolution and model covariance matrices are good approximations to the true model resolution and model covariance.

Day-Lewis and Lane (2004) investigate the effects of regularization on tomograms from a geostatistical distribution of velocities in their model. Their analysis uses the straight ray approximation to linearize the problem. They conclude that the statistical distribution of the velocities is strongly dependent on the regularization, as well as the data error, acquisition geometry, and the size of the heterogeneity (Day-Lewis and Lane, 2004).

In this paper, I address the effects of parameter choice on the inverted velocity model. Through plots showing the results of different parameter choices, one can better understand the effects of these choices and thus more easily recognize artifacts from the inversion. Day-Lewis and Lane (2004) state that "two tomograms inverted from a given data set can differ markedly in structure depending on the chosen regularization criteria." Other choices, such as the starting model and the reference model may effect the model structure too.

Many studies, for example Chang *et al.* (2004), are evaluating the attenuation of EM energy to better understand the physical property distribution in the subsurface. Although I am using traveltime tomography as my example, the results of this study should be applicable to attenuation tomography studies too.

As a first step towards addressing these questions, I investigate some basic sources of uncertainty in the tomographic inversion step. I start with a known test model, simulate a tomography experiment, and invert the synthetic traveltimes. Comparing the inversion results with the known input model can improve our understanding of the capabilities and limitations of different tomographic methods. I also have many different models from the same traveltimes. These different models provide a range of acceptable models from which to infer the robust model features.

I do not address error associated with borehole deviation or the mis-location of the antennas in the well. Although these errors effect the tomogram, they will not effect the choice of model parameterization. I include noise in the traveltime picks to more realistically simulate field data. This noise effects the choice of parameterization in two ways. First, the stopping criteria for the iterative solution is based on the data noise. Secondly, regularization is used to prevent overfitting the data. The inversion algorithm introduces structure in the model to fit the traveltime picks. Since the data contain noise, the inversion adds structures to fit the noise in the data. By regularizing the inversion, for example through flatness or smoothness constraints, the inversion method will try to find models with less structure, yet fit the data to within the error tolerance.

I look at the forward model operator, the effects of noise, the regularization, the reference and starting model, the discretization, and the angular coverage of the data. I used two different inversion algorithms to show the influence of the forward operator: one straight ray and one curved ray. I look at the effects of increasing the noise in the traveltime picks, as well as different types of noise distributions. I next look at the effects of model regularization. I use two simple regularization schemes with different amounts of weighting. Another important parameterization decision is the reference and starting model. How do the choices effect the inverted model? The resolution of the inverted model is tied to the grid size used in the inversion. Is it preferable to use a small grid size to be sure to model small features? Or does a small grid size introduce artifacts? Does using a large grid size miss important features in the subsurface? Finally, an important aspect of the data is the angular coverage of the interwell area. High-angle rays are necessary to correctly locate lateral velocity variations in the subsurface. However, these high-angle rays may also introduce artifacts into the model. What features are artifacts caused by the high-angle rays? By presenting many models from the same traveltimes but with different parameterizations, I hope to demystify some of the ''art'' in tomography for new users of the technique.

Background Theory

Matrix algebra provides a convenient way to express forward and inverse problems such as traveltime tomography. The forward problem is

$$\mathbf{d} = \mathbf{G}\mathbf{m}, \tag{1}$$

where $\mathbf{d}$ is the data (vector), $\mathbf{G}$ is the kernel function (matrix), and $\mathbf{m}$ is the model (vector). The kernel function projects the model onto the data space. The kernel function represents the physics of the problem, including boundary conditions and differential equations, and is generally not square.

A solution to the inverse problem is

$$\mathbf{m} = \mathbf{G}^{-1}\mathbf{d}. \tag{2}$$

Conceptually, the inversion process involves computing the inverse of matrix $\mathbf{G}$ and then multiplying this matrix by the data to compute the model. Typically, $\mathbf{G}^{-1}$ is impossible to compute, because the matrix is ill-posed, ill-conditioned, or large. A weighted, damped, least squares approach is often used to find a solution (Menke, 1989). In the weighted, damped, least squares approach to inversion, I use an L2 norm to determine the optimal solution from the objective function

$$\begin{aligned}\min\Big\{&(\mathbf{d} - \mathbf{G}\mathbf{m})^{\mathrm{T}}\mathbf{W}_{\mathbf{d}}^{\mathrm{T}}\mathbf{W}_{\mathbf{d}}(\mathbf{d} - \mathbf{G}\mathbf{m}) \\ &+ \lambda(\mathbf{m} - \langle\mathbf{m}\rangle)^{\mathrm{T}}\mathbf{W}_{\mathbf{m}}^{\mathrm{T}}\mathbf{W}_{\mathbf{m}}(\mathbf{m} - \langle\mathbf{m}\rangle)\Big\},\end{aligned} \tag{3}$$

where $\langle\mathbf{m}\rangle$ is the starting and reference model, $\mathbf{W}_{\mathbf{m}}$ is the regularization matrix, $\mathbf{W}_{\mathbf{d}}$ is the data weighting matrix, and λ is the weighting factor between data misfit and solution length. The parameter λ determines how much the data influences the model versus how much the regularization constrains the model. For $\lambda = 0$, the solution depends only on the data. For very large λ values, the solution depends on the regularization. Taking the derivative with respect to the model parameters, $\mathbf{m}$, and setting the result to zero, yields the weighted, damped, least squares solution (Menke, 1989):

$$\begin{aligned}\mathbf{m}_{\mathbf{est}} = \langle\mathbf{m}\rangle &+ \left[\mathbf{G}^{\mathrm{T}}\mathbf{W}_{\mathbf{d}}^{\mathrm{T}}\mathbf{W}_{\mathbf{d}}\mathbf{G} + \lambda\mathbf{W}_{\mathbf{m}}^{\mathrm{T}}\mathbf{W}_{\mathbf{m}}\right]^{-1} \\ &\times \mathbf{G}^{\mathrm{T}}\mathbf{W}_{\mathbf{d}}^{\mathrm{T}}\mathbf{W}_{\mathbf{d}}[\mathbf{d} - \mathbf{G}\langle\mathbf{m}\rangle]\end{aligned} \tag{4}$$

where $\mathbf{m}_{\mathbf{est}}$ is the best fitting model. In the tomography

problem, the data are first arrival times and the algorithm tries to minimize the difference between the data misfit and the solution length.

A variety of computational methods have been developed to implement matrix inversions, including an algebraic reconstruction technique (ART) (Peterson et al, 1985), a simultaneous iterative reconstruction technique (SIRT) (Tweeton, 1988), or an iterative conjugate gradient-like solver (LSQR) (Paige and Saunders, 1982). These methods find the solution through iteration. I use a straight ray tomographic inversion using SIRT (Tweeton, 1988) and a curved ray inversion using LSQR (Aldridge and Oldenburg, 1993). The curved ray inversion is nonlinear. Linearizing the problem results in an iterative method to solve the tomography problem.

Synthetic Model

To test the different crosshole traveltime tomography parameterizations, I used a finite-difference approximation to Maxwell's equations (Lampe *et al.*, 2003) to simulate a crosshole radar tomography experiment. The finite-difference method calculates the wavefield propagating through a gridded velocity field. Figure 1 shows the test velocity model and traveltimes from two source locations. The model simulates air, the vadose zone, and lateral changes in the saturated zone to test the inversion algorithms' ability to image features common in near surface investigations. The test model includes vertical and horizontal velocity changes. I have developed the test model based on gravel outcrops and a research well site near Boise, ID (Barrash and Clemo, 2002; Tronicke *et al.*, 2004; Clement *et al.*, 2006). The simple layering is chosen to be more representative of sediment outcrops than the stochastic physical property distributions used in transport problems. The velocities were selected to represent the velocity distribution derived from GPR studies at the research well site (Clement *et al.*, 2006; Tronicke *et al.*, 2004). From these studies, the vadose zone has a velocity of about 0.14 m/ns. The velocities in the saturated zone vary from a low of about 0.06 m/ns to a high of about 0.1 m/ns. The water table is at about 2 m.

The model is 5 m by 10 m with a horizontal and vertical grid spacing of 0.05 m. I included several layers, some with lateral velocity changes, to simulate the types of features often observed in the subsurface. The test velocity model consists of high and low velocity zones and thick and thin layers to test the inversion schemes. Above the top layer of the model, the velocity is 0.3 m/ns to simulate air. The air layer is included to model refractions at the air-surface interface. The upper, 2 m thick layer, represents the vadose zone with a velocity of 0.140 m/ns. Velocities in the simulated saturated zone

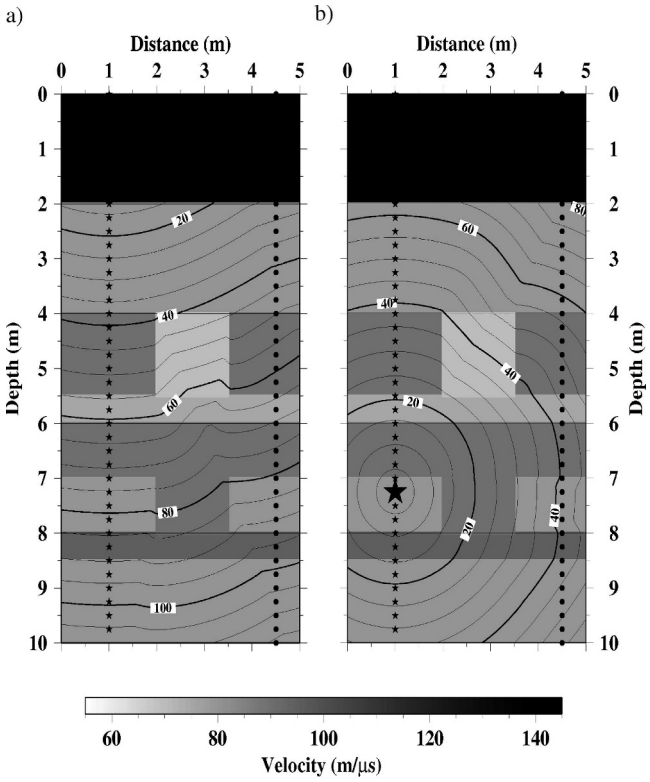

Figure 1. Test model used to generate the synthetic travel times. The wells are located at 1.0 m and 4.5 m. The small stars indicate the sources used to generate the synthetic travel times. The dots are the receiver locations. The contoured lines are the travel times for a source located a) at 0.25 m and b) at 7.25 m depth.

(2–10 m depth) range from 0.070 to 0.095 m/ns. Layers are horizontal and range in thickness from 0.5 to 2.0 m. The layer at 4.0 to 5.5 m depth contains a low-velocity inclusion near the center of the model, between 2.0 and 3.5 m on the horizontal scale; at the edges of the layer the velocity is 0.090 m/ns whereas the velocity is 0.070 m/ns in the inclusion. A high-velocity zone is included in the layer between 7.0 and 8.0 m depth. Close to the wells, the velocity is 0.080 m/ns whereas near the center, again between 2.0 and 3.5 m on the horizontal scale, the velocity is 0.090 m/ns. These horizontal velocity changes are included to determine the ability of the inversion methods to image heterogeneity in the subsurface. The synthetic modeling results in this paper provide insight into the capabilities and limitations of different tomography methods and the level of detail that can be reliably interpreted from tomographic images.

I simulated a traveltime tomography experiment in two wells spaced 3.5 m apart (Fig. 1). First arrival travel times were picked from the synthetic wavefield comput-

ed between 40 shot locations spaced 0.25 m down the well and 41 receiver locations also spaced at 0.25 m intervals. To get accurate picks, I computed the first arrival travel times using a finite-difference eikonal equation forward model (Hole and Zelt, 1995), similar to the forward model used in the inversion algorithm. I then superimposed these travel times onto the simulated crosshole tomography waveforms to be sure the travel times were accurate. The picks aligned with the first arriving energy in the waveforms. The simulated tomographic traveltimes consists of 1640 travel time observations.

Results of Inversion

I used two different inversion routines to invert the synthetic crosshole traveltimes. The curved ray inversion method uses a finite-difference approximation to the eikonal equation (Aldridge and Oldenburg, 1993; Vidale, 1990). This algorithm can incorporate ray bending at velocity contrasts, such as the air/ground interface or the vadose/saturated zone interface. The routine linearizes the system and finds a solution using LSQR (Paige and Saunders, 1982). I also used a straight ray inversion method that uses straight ray paths between the sources and the receivers (Tweeton, 1988). This routine solves the linear system of equations using a SIRT algorithm.

Except for the comparison of straight ray to curved ray inversion, the analysis uses the curved ray inversion method. To make a comparison between different parameterizations, I tried to keep the inversion parameters consistent when possible. I used a 0.1 m grid size for the inversion. I stopped iterating to the solution when the RMS residual was less than or equal to 0.5 ns or the number of iterations exceeded 25, except for the noise and grid size analysis. The 0.5 ns stopping criterion is based on the noise distribution in the simulated traveltimes, which is discussed in more detail later. All the inversions stopped before the 25 iteration limit.

The LSQR algorithm iterated until the relative error increment was less than 1×10^{-6} or the number of iterations was greater than 150. The small relative error increment ensures that the LSQR algorithm is near the solution. The 150 iteration limit gives the LSQR algorithm sufficient iterations to find the solution. After that number of iterations, the algorithm will probably not find the solution.

The initial starting model and the reference model were the same in each inversion. For all the inversions, except for the regularization analysis, I used a model weight of 0.01 and a flatness constraint weighted by 15 in the horizontal direction and 5 in the vertical direction. The model weight damps the instability in the inversion due to small eigenvalues. Adding a small value to the eigenvalues stabilizes the inverse procedure. I chose the horizontal and vertical weights based on my expectations of the model. In outcrops, the layering is more continuous in the horizontal direction than in the vertical direction. I used a small scalar value to minimize the reference model influence. Large scalar weight values force the solution to minimize the solution length at the expense of the data misfit.

Except for the starting and reference model analysis, the curved ray inversion used a two-layer starting model with a velocity of 0.140 m/ns in the upper 1.8 m, a 0.08 m/ns velocity below 2.2 m, and a linear velocity gradient between 1.8 to 2.2 m. This model is based on a simple, two-layer velocity structure; a vadose zone and a saturated zone. In the vadose zone, air fills the pore spaces, resulting in a faster velocity than the water-filled pores of the saturated zone. The velocity gradient represents the capillary fringe, but is also included to allow the finite-difference algorithm to more accurately compute the travel times.

Straight Ray versus Curved Ray

The straight ray inversion uses a different method to regularize the solution. The inversion finds a weighted average of the model parameters based on the cell value and its neighbor parameter values. The curved ray method uses Tikhonov regularization that imposes a flatness constraint as previously mentioned. Also, the straight ray inversion is linear so the inversion does not iterate to find the solution, but iterates the SIRT algorithm to solve the system of equations until the stopping criterion is met.

Figure 2 shows the test model and a comparison of the straight ray and curved ray inversions using noise-free traveltimes. In general, models from either method are similar and image the velocity changes in the test model (Fig. 2). The curved ray inversion (Fig. 2c) is better able to define the test model boundaries than the straight ray inversion (Fig. 2b). Figures 2d–e show the differences between the two models and between the test model and each inverted model.

Both methods poorly image the upper 2 m. The simulated energy is strongly refracted at the air-surface boundary at 0 m and at the 2 m depth boundary. For the straight ray case, straight rays are a poor approximation to the true ray path across these boundaries resulting in the highly variable velocities in this zone. Not surprisingly, the curved ray inversion better images the 2 m depth boundary. However, the velocity in this zone is different from the test model. The curved ray inversion has a two layer model for the upper 2 m. Between 0 to 1 m, the velocities are very fast, much

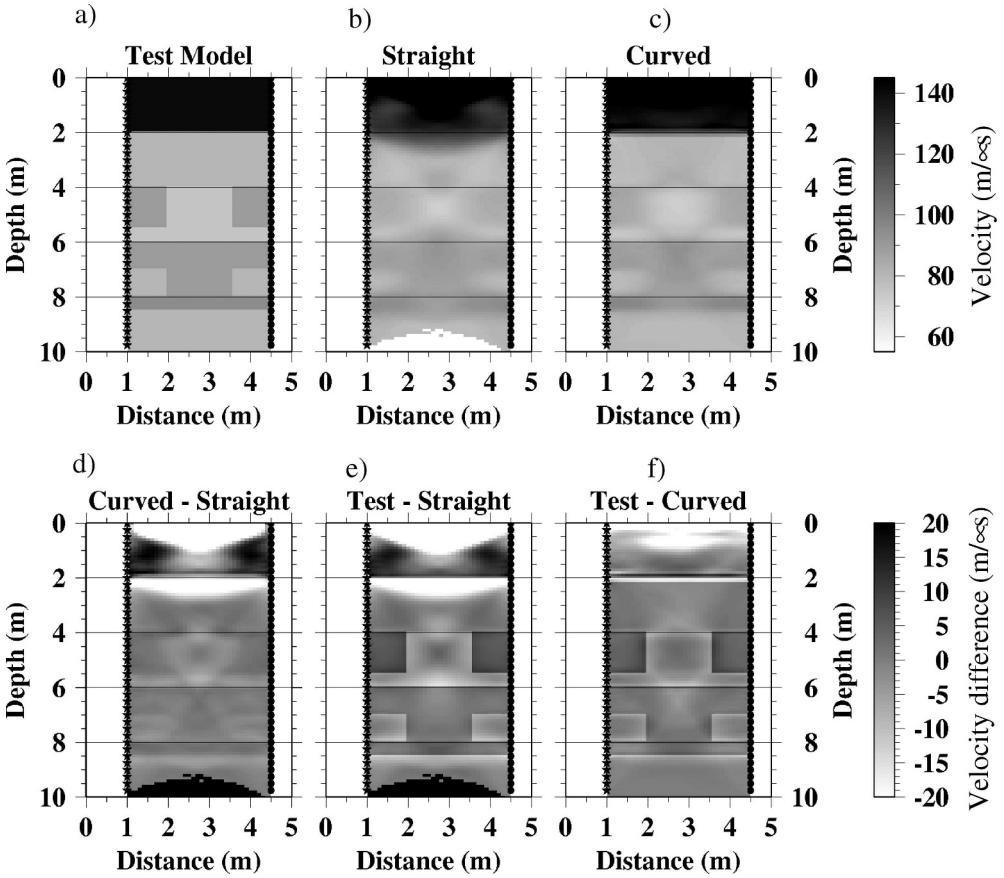

Figure 2. A comparison of the straight ray and the curved ray algorithms using noise-free traveltimes. a) True model used to generate the synthetic travel times. b) Inverted model using the straight ray inversion algorithm. c) Inverted model using the curved ray algorithm. d) The difference between the curved ray model minus the straight ray model. e) The difference between the test model and the straight ray model. f) The difference between the test model and the curved ray model.

faster than the 0.16 m/ns maximum velocity displayed in the Figure 2. Between 1 to 2 m, the velocity is similar to the 0.14 m/ns velocity of the test model, although the modeled velocity is faster than 0.14 m/ns. The poor image in this region is probably due to the large velocity contrasts in the model: from 0.3 m/ns to 0.14 m/ns at 0 m depth and from 0.14 m/ns to 0.08 m/ns at 2 m depth. These large velocity changes are difficult for the finite-difference solver to properly model (Hole and Zelt, 1995; Podvin and Lecomte, 1991). Figure 3 shows the ray density plots for both inversions. The ray density is the number of rays through a cell divided by the length of the cell. High ray densities indicate well-sampled cells and low ray densities indicate poorly-sampled cells. The zone above 2 m, especially between 0 to 1 m, is poorly sampled by the rays. Structures near regions of large velocity changes may be artifacts of the forward operator, not model features required by the data.

Throughout this analysis, the inversions poorly image the upper 2 m and the discussion will focus primarily on the inverted models below 2 m.

In the straight ray model, the low-velocity anomaly between 4 to 5.5 m depth is not as well imaged as in the curved ray model. An X-pattern is apparent in the velocity model between 3 and 6 m depth. This X-pattern is common in straight ray inversions. The forward model, **G**, maps the errors in the model onto the data (Oldenborger *et al.*, 2005). The straight ray forward model smears the errors along the diagonal straight-ray paths resulting in the X-pattern.

The curved ray inversion resolves the thicknesses of the layers better than the straight ray algorithm. The X-pattern is less apparent; the velocity boundaries are sharper at 4, 5.5, and 6 m. The curved ray model also more clearly shows the lateral velocity changes in the center of the domain, although the boundaries of the inclusions are blurry.

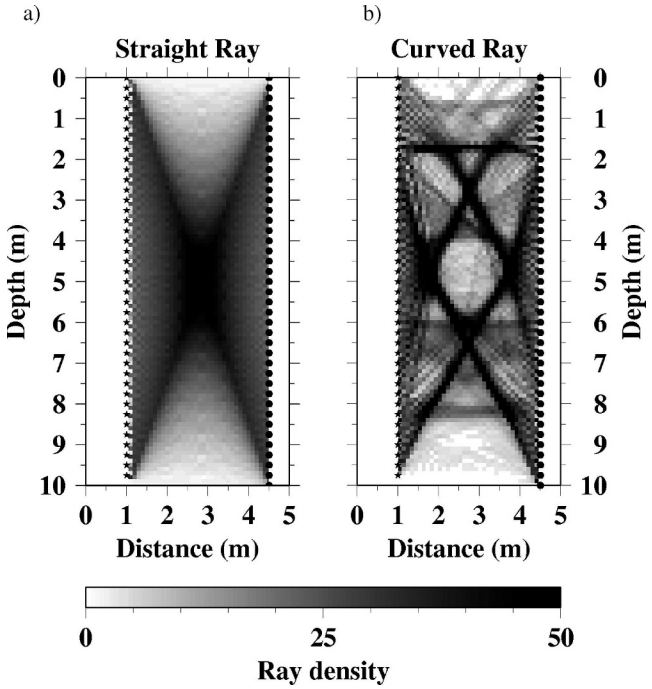

Figure 3. Ray density diagram. a) Ray densities from the straight ray inversion. b) Ray densities from the curved ray inversion.

The two inversions fit the traveltimes about the same. The straight ray inversion converges to an RMS misfit of 0.494 in 16 iterations. The model has a velocity range of 0.057 to 0.177 m/ns, greater than the true range. The mean residual is 0.059 ns with a range of −2.46 to 1.83 ns. The curved ray inversion converges in 4 iterations to an RMS misfit of 0.491 ns. The inversion fits 1637 of the 1640 travel times. The model has a velocity range of 0.069 to 0.300 m/ns, wider than the straight ray velocity range. The residuals for the curved ray model have a mean of −0.002 ns with a range of −2.195 to 2.122 ns. Both methods have an average error near zero, but the curved ray method has a smaller RMS error indicating a smaller width in the misfit error distribution despite having a wider range.

Subtracting the inverted models from each other and from the test model shows the degree to which the models differ (Fig. 2d–f). In the difference plots, the region above 3 m depth has the largest discrepancy from the test model, especially for the straight ray tomography. Between 3 and 9 m, the straight ray and curved ray models are similar to the test model and are nearly the same to each other.

The difference of the curved ray model and the straight ray model has an RMS value of 9.64 m/μs, with a range of −87.01 to 45.38 m/μs. The small RMS value indicates that the models are very similar. The difference of the straight ray model from the test model has an RMS value of 9.64 m/μs with a range from −99.51 to 45.00 m/μs. The difference of the curved ray model from the test model has a lower RMS value, 5.09 m/μs and a narrower range, −89.64 to 14.79 m/μs, than the test model minus the straight ray model and the curved ray model minus the straight ray model. If I restrict the analysis to depths between 3.0 and 9.0 m, where fewer artifacts exist, the RMS values of the differences between the test model and the inverted models are smaller and the ranges are much narrower. For the test model minus the curved ray model, the RMS value is 2.80 m/μs and the range is −11.27 to 9.93 m/μs. For the test model minus the straight ray model, the RMS value is 4.53 m/μs and the range is −15.62 to 45.00 m/μs. For the curved -straight ray case, the RMS value is 2.34 m/μs and the range is −8.09 to 45.38 m/μs. The small RMS value still indicates that the models are closely matched. Both the straight ray and the curved ray tomography provide velocity models that distinctly image the main features in the test model.

To gain insight into how the two inversion methods partition error along ray paths, I generated plots of ray density for both methods (Fig. 3). For the straight ray inversion, more rays pass through the center of the model than at the edges. The ray density decreases systematically away from the model's center, with few rays sampling the top and bottom of the model. This coverage difference will cause the inversion algorithm to assign errors to the less densely sampled cells because they affect fewer of the travel times. (Some of the error in the less densely sampled cells also comes from the regularization). Thus, the edges of the model are less constrained than the middle and, consequently, the uncertainty is greater for the edges. From the ray density, I have more confidence in the modeled features in region between 3 to 7 m depth and 2.0 to 3.5 m distance.

The curved ray inversion has a much different ray density character. Thin zones of higher ray density exist in the model. High ray density zones extend horizontally, most notably at 1.5 to 2.0 m, but also at 8.0 to 8.5 m depth. Diagonal zones of high ray density also exist in the plot. These high ray density zones roughly correspond to the high velocity zones in the test model. Zones of low ray density roughly correspond to low velocity regions. These low velocity regions are poorly sampled by the rays and consequently, the inversion has difficulty resolving these features. As in the straight ray case, few rays sample the top and bottom of the model.

I also computed estimates of the resolution and covariance matrices of the curved ray inversion. Resolution is a measure of the averaging from neighboring cells used to calculate the cell value. A well

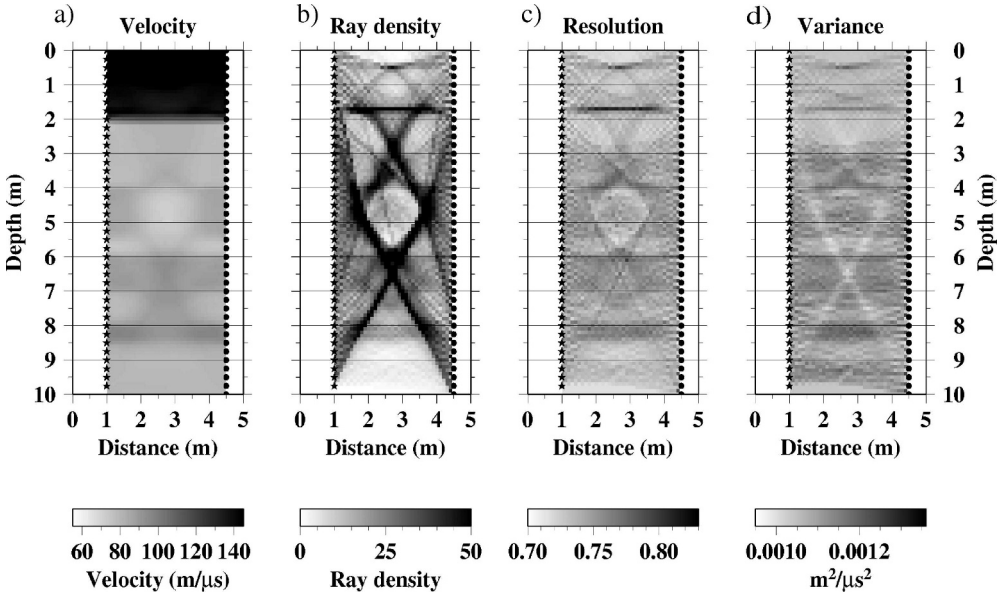

Figure 4. Resolution and variance estimates compared to the ray density. The resolution values are the diagonal elements of the full resolution matrix. The variance values are the diagonal elements of the covariance matrix.

resolved cell will have a value near 1 with small side lobes away from the diagonal. Covariance is a measure of the uncertainty in a particular value. The diagonal elements of the covariance matrix are the variances. Although the resolution and covariance matrices are formally defined only for linear inversions, Nolet *et al.* (1999) developed a method for determining the diagonal elements of the resolution and covariance matrices from nonlinear inversions. Figure 4 compares the ray density to the diagonal elements of the resolution and covariance matrices from the curved ray inversion. The diagonal value for the resolution matrix and the variance for a cell is plotted in Fig. 4c and 4d at the cell's location. The mean value of the diagonal resolution elements is 0.72 with a standard deviation of 0.04. The mean value of the variance is 0.0011 $\mu s^2/m^2$ with a standard deviation of 0.0001 $\mu s^2/m^2$. The resolution and ray density plots are similar in structure; more well resolved regions tend to correspond to higher ray densities. The high velocity regions have larger resolution values than the low velocity regions. The top and bottom of the model also has low resolution. These are areas of low ray density.

The variance plot is also similar to the resolution plot; for the most part, higher variances correspond to higher resolution values. This correlation indicates that the model values for well resolved features are less well known. An exception is the X-pattern in the plots between 2 to 9 m depth. The ray density and resolution plots have high values, whereas the variance plot has small values. The X-pattern region has a much higher ray density, well over 50, than the rest of the model. This inverse relationship between the ray density and the variance indicates that the highly sampled regions of the model have small uncertainty in their estimated values. From the information in Fig. 4, the most reliable estimates of the model values are the areas where the model is highly sampled.

The resolution and variance analysis shows an important difference between straight ray and curved ray inversions. Both methods image the main features of the test model. However, if model appraisal is important, then a different reliability assessment will result from the two methods. The ray density from the straight ray inversion implies that the more certain features are at the center of the model and the reliability decreases from the center. The curved ray inversion ray density implies that layer boundaries and high velocity zones are more reliable than the rest of the model, especially the low velocity zone.

The different ray tracing routines in the inversions account for the different inverted velocity models. The curved rays more accurately model the true ray paths. The wave fronts in Fig. 1 refract and bend at the velocity contrasts. The ray paths are clearly not straight. Boundaries are sharper and velocity changes are more distinct in the curved ray model. The ray coverage in the curved ray method shows that more rays are concentrated along the high velocity zones in the model, especially along large velocity contrasts.

The rest of the analysis will use the curved ray inversion method.

Table 1.

Standard deviation (ns)	Mean residual (ns)	RMS residual (ns)	Minimum residual (ns)	Maximum residual (ns)
Noise-free	0.082	0.319	−1.787	1.705
0.1	0.029	0.247	−1.267	1.184
0.4	−0.002	0.491	−2.195	2.211
1.0	0.064	0.997	−4.057	4.281
2.0	0.002	1.989	−8.303	8.645

Effect of Noise

A crucial parameter in iterative tomographic inversion is the noise tolerance or stopping criterion. When the value of the objective function (Eq. 3) is less than a selected tolerance, the inversion stops. If the value of the objective function is much smaller than the noise level, the model has over-fit the data. In this case, the model contains features that are necessary to fit the noise in the data. The stopping criterion is ideally set to some measure of the noise level in the data. One such measure of the noise level is the standard deviation of the noise. For the curved ray inversion, the iterations stop when the root mean square (RMS) traveltime residual is less than the stopping criterion.

To investigate the effect of noisy data, I generated four traveltime sets with added Gaussian random noise distributions to compare with the noise-free travel times. The noisy traveltime sets had a mean of 0 with standard deviations of 0.1 ns, 0.4 ns, 1.0 ns, and 2.0 ns. I also randomly added or subtracted 0.5 per cent of the total traveltime of the arrival to increase the traveltime error with increased traveltime, a more realistic noise distribution. Table 1 lists statistics on the residuals from the different inversions. I set the stopping criteria for the 1.0 and 2.0 ns added noise cases to the standard deviations, 1.0 and 2.0 ns respectively. For the 0.1 ns added noise case, the inversion routine stopped after reaching the imposed 25 iteration limit. The RMS residual oscillated about a 0.22 ns, greater than the 0.1 ns criterion. So that the routine converged, I set the stopping criterion to 0.25 ns. The inversion also stopped after the 25 iteration limit for the case of added noise with a standard deviation of 0.5 ns. In this case, instead of changing the stopping criterion, I added noise with a 0.4 ns standard deviation to the traveltimes. With this level of noise, the inversion converged to the 0.5 ns stopping criterion. In all cases, the inversions converged to the stopping value after no more than 7 iterations.

Figure 5 shows the inverted models from the different standard deviations. As the amount of added noise is increased, the images are less like the test model. When the added noise is greater than 0.4 ns, the models are a poor image of the test model. Although the features are apparent in the 1.0 ns standard deviation case, without the test model for comparison the features would probably be misidentified. The models from less noisy traveltimes adequately image the main features of the test model.

I also generated non-Gaussian random noise distributions (Fig. 6) to test the curved ray algorithm. One set of arrivals has random noise added with a Laplace distribution. The Laplace distribution has a 0 ns mean and a width of 0.28 ns. The third set of noisy arrivals have added random noise with a gamma distribution. The gamma distribution has two parameters, the order and the width. I use a third order gamma function with a width of 0.12. I chose the widths for the Laplace and gamma distributions to have approximately the same standard deviation, defined as the square root of the second moment about the mean, as the Gaussian distribution. The Laplace and gamma distributions had standard deviations of 0.395 ns.

The results for the different noise distributions are shown in Fig. 7. The inverted models are similar. The three models with noise have a more varied velocity distribution within constant velocity zones than the noise-free traveltimes, but all four models image the features in the test model. The type of noise distribution does not change the inverted model significantly. Non-gaussian noise traveltimes do not seem to effect the ability of the inversion method to image the features of the test model.

For the rest of the analysis, I will use traveltimes with added Gaussian noise with 0 mean and a 0.4 ns standard deviation.

Effects of Regularization

I also investigated the use of different types of regularization as constraints for the curved ray inverse procedure. I inverted the traveltimes with added Gaussian random noise using flatness (first difference, -1 1) and smoothness (second difference, 1 -2 1) constraints (Aldridge and Oldenburg, 1993). The flatness constraint seeks to find the model without velocity changes. In other words, I want a solution with as little lateral change as possible. The smoothness constraint seeks to minimize the gradient of the velocity change in the designated direction. That is, I want a solution that has small changes in velocity gradient.

I used nine different regularization constraints, listed in Table 2, to analyze the effects of different regularization schemes. The regularization weights can be varied in the horizontal and vertical directions by a scalar. I tested schemes that weighted the horizontal direction, the vertical direction, and both directions. I chose scalar values of 5, 15, 25, or 50. These values were

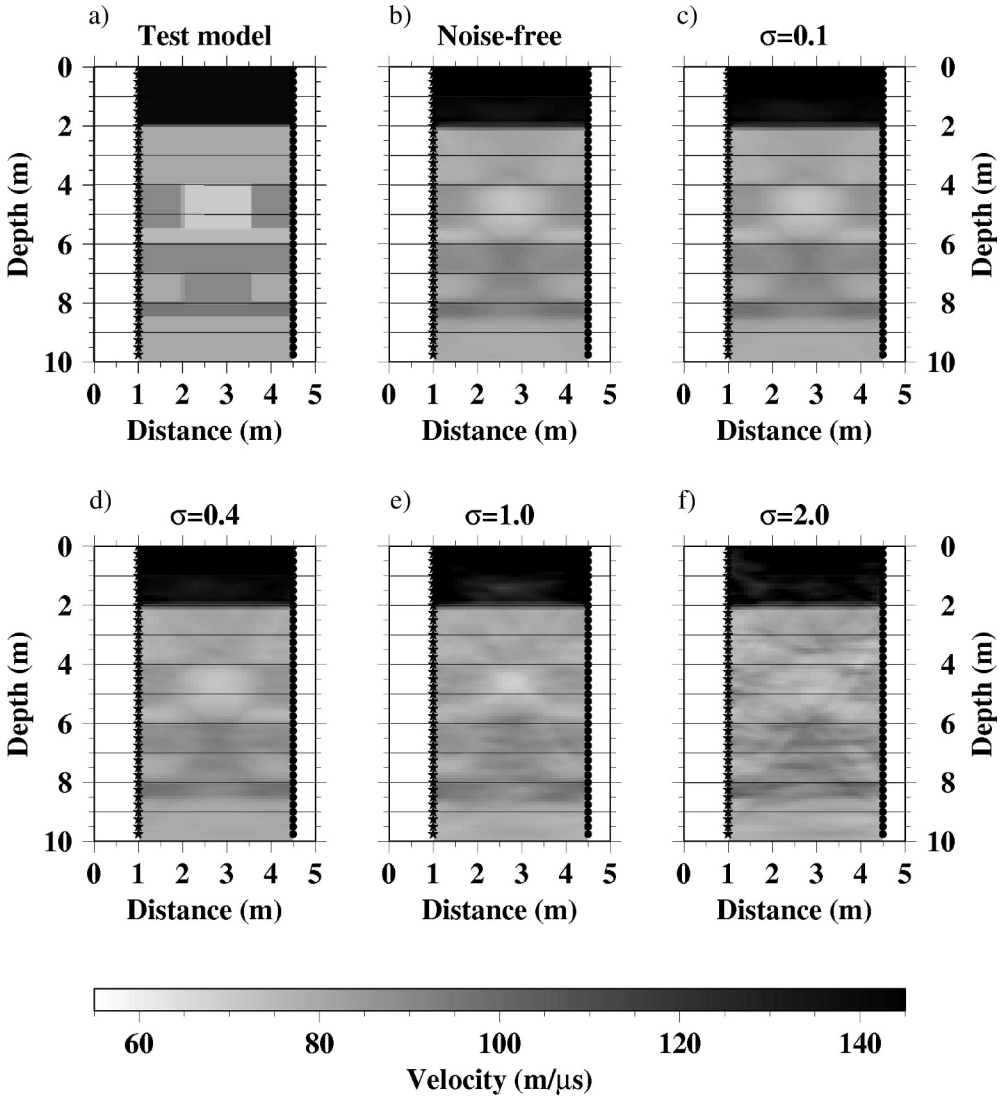

Figure 5. Inversions for the noise-free traveltimes and for traveltimes with added random Gaussian noise with a 0 mean and different standard deviations: a) Test model, b) Noise-free, c) 0.1 ns standard deviation, d) 0.4 ns standard deviation, e) 1.0 ns standard deviation, and f) 2.0 ns standard deviation.

sufficient to constrain the inversion without imposing too much structure. I tried inverting without weighting in one direction, for example, (25, 0). However, not weighting in both directions caused the forward modeling step to fail to trace rays between all the source-receiver pairs. The smoothness regularization schemes converged within 10 iterations. The flatness constraints with equal weighting and strong weighting in the vertical direction did not converge to the 0.5 ns RMS residual value within 25 iterations.

Figure 8 shows the results of the different regularization constraints in the curved ray inversion. The inverted velocity models are similar and adequately image the main features of the test model. Strongly horizontally regularized models (8b, 8d, 8f, and 8h) appear to have short, discontinuous layers within the larger layered zones. The strongly vertically constrained models (8c and 8g) show a variation in the horizontal direction, especially above 2 m and below 6 m. The velocity variations within layers appear greater in the smoothness models than the flatness models. The boundaries of the layers in the smoothness models are less horizontal than in the flatness models. The flatness regularization with 15 horizontal and 5 vertical weighting is the best choice for this test model.

A method of assessing the uncertainty in the inverted result is to find many models and compute the average model and its standard deviation. Figure 9 compares the test model, the model with a (15, 5) flatness constraint, the average of the 9 regularization

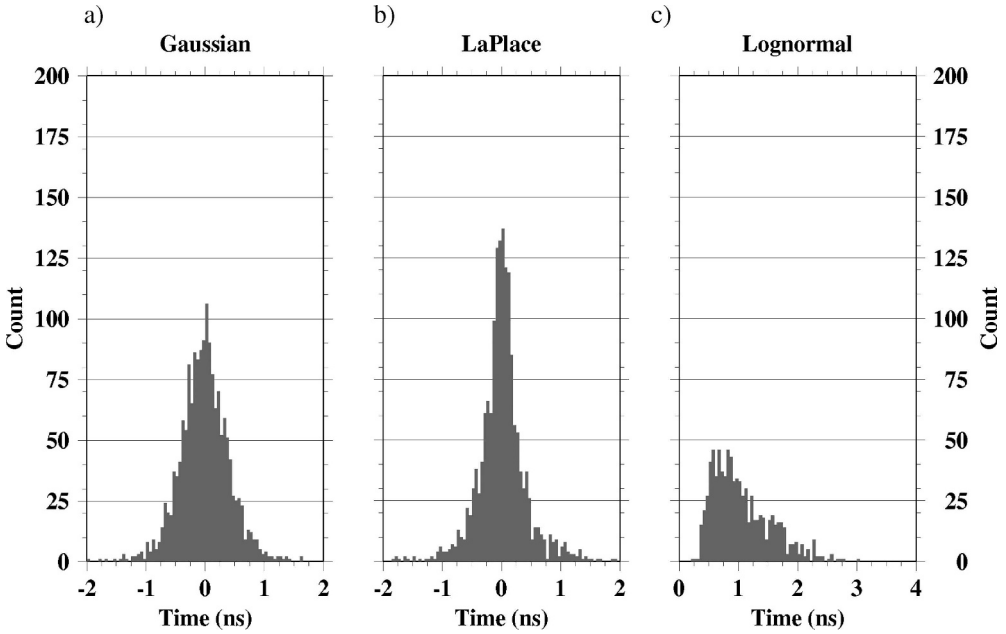

Figure 6. Histograms of the added random noise. The different distributions have approximately the same widths.

models, and their standard deviation. The average model looks similar to the flatness model. The standard deviations in the upper 2 m are mostly less than 15 μs/m. Below 2 m, the standard deviations are smaller, less than 3 μs/m. Based on Fig. 9c and 9d, the features in the average model below 2 m are reliably determined.

Importance of Starting Model

Another important parameter for curved ray tomographic inversions is the starting model for the nonlinear inversion. The curved ray inversion routine traces rays through the starting model, then alters the model to reduce the misfit error. A danger in this iterative method is that the routine finds a local

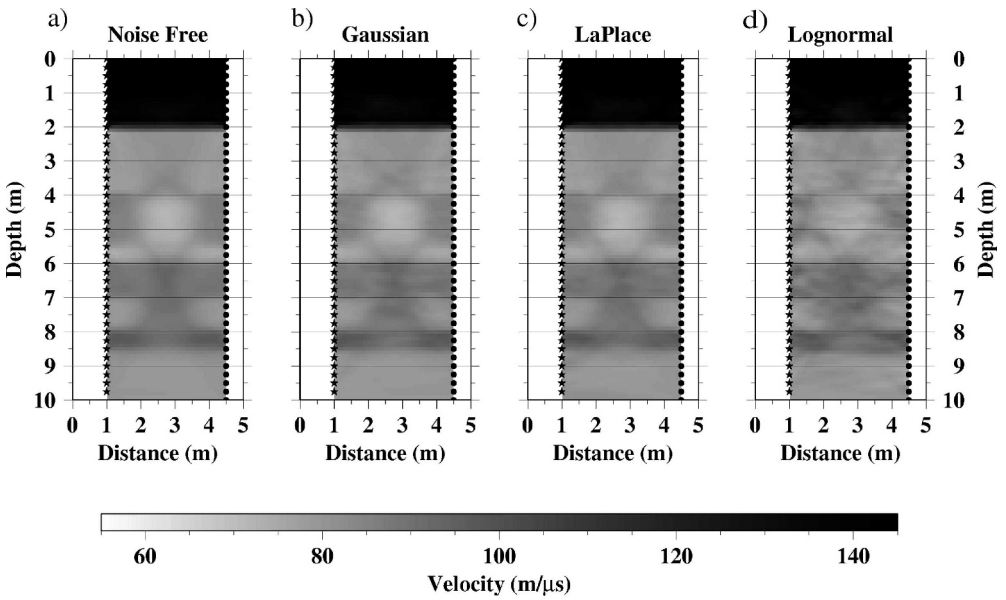

Figure 7. Noise-free versus noisy travel times. a) Inverted model using noise-free travel times. Inverted model using travel times with noise added to simulate realistic data: b) Gaussian distribution, c) LaPlace distribution, and d) Lognormal distribution.

Table 2.

Weights (Hor., Ver.)	Flatness	Smoothness
25, 5	yes	yes
5, 25	yes	yes
25, 25	yes	yes
15, 5	yes	yes
50, 50	yes	no

minimum rather than the global minimum solution. The inversion routine uses the starting model to compute an objective function value. One hopes this objective function value is sufficiently close to the problem's global minimum that the inversion converges to this global minimum and not to a local minimum. To test that the solution is the global minimum of the objective function, I inverted the traveltimes using several different starting models (Fig. 10). Table 3 lists the velocities for the starting models except for the ZOP and the Test-Average case. Models 1 through 5 are constant velocity models; models 6 through 8 are two-layer models with the velocity gradient occurring between 1.8 to 2.2 m depth. Curved ray algorithms perform better with velocity gradients instead of sharp contrasts. The ZOP model is derived from the simulated zero offset profile experiment. A ZOP experiment consists of travel times recorded when the transmitter and receiver are at the same depth. I derived the Test-Average model by averaging the velocities from the test model horizontally and weighting by the horizontal distance of the velocity layer in the model.

The resulting tomograms are similar (Fig. 11), suggesting that the solution is well behaved. A noticeable difference between the homogeneous models and the two-layered models occurs at 2 m depth. The inversion better images the large velocity contrast at 2 m when the starting model includes such a discontinuity. The ZOP result is the most different. The inverted model contains a gradient at 2 m similar to the homogeneous models. However, a thin, lower velocity layer occurs at 3 m depth, coinciding with the base of the gradient zone in the ZOP starting model. This layer is the most significant difference from the test model. This layer could be interpreted as an additional layer not

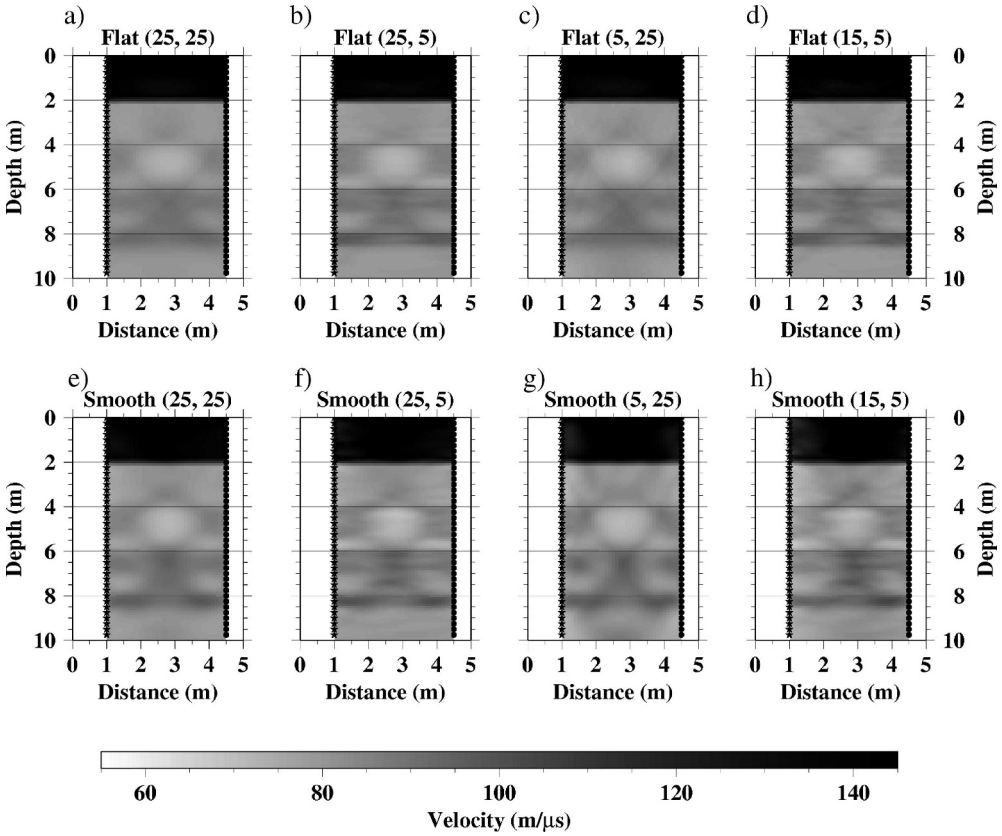

Figure 8. Effects of the regularization constraints. The inverted travel times contain Gaussian noise. The top row shows models with a flatness constraint. The bottom row shows models with a smoothness constraint. The models are aligned vertically such that constraints with similar weighting are paired.

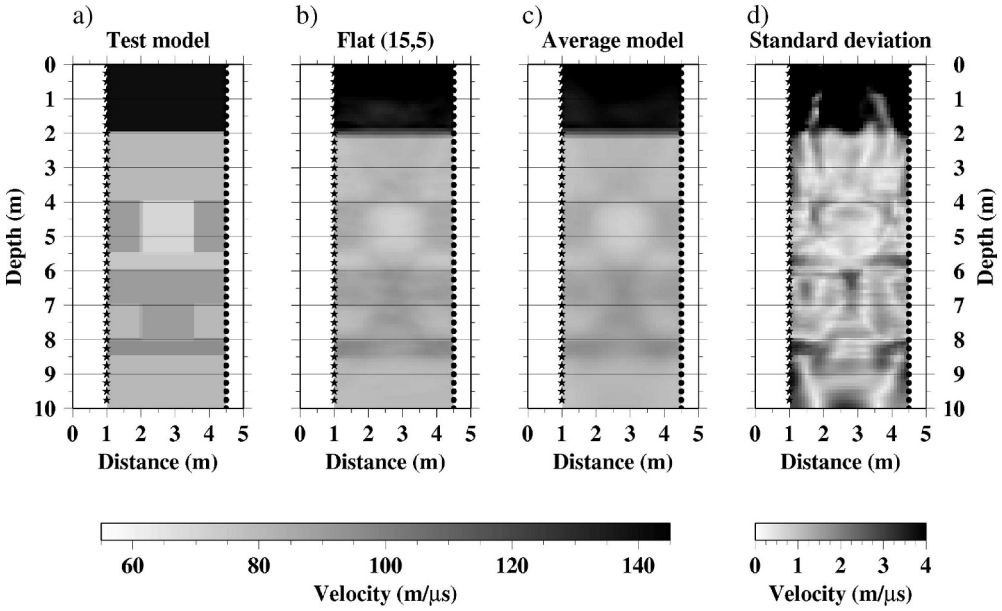

Figure 9. Average of regularization constraints. a) The test model; b) the model inverted with a flatness constraint of 15 horizontally, 5 vertically; c) the average of the 9 regularized models; d) the standard deviations from the average model. The gray scale for the standard deviations is scaled to emphasize the variation in the lower 2 m. In all the models, black indicates values greater than or equal to the largest value. The range in the gray scale was chosen to show the variation in standard deviations below 2 m.

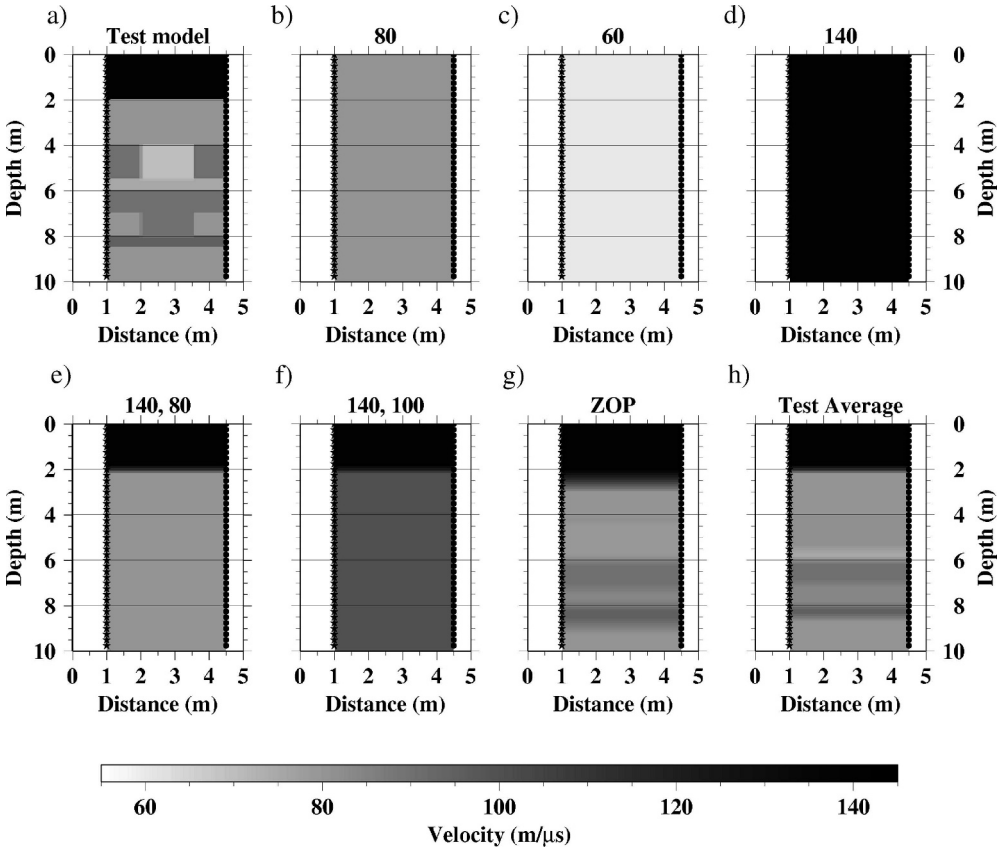

Figure 10. Selected starting models used to assess the dependence of the inversion on the choice of starting model. The test model is shown for comparison.

Table 3.

Model	Velocity m/ns
1	0.08
2	0.06
3	0.10
4	0.04
5	0.14
6	0.14, 0.08
7	0.14, 0.10
8	0.14, 0.06
9	ZOP
10	Test-Average

present in the test model. Surprisingly, the increased detail and accuracy of the Test-Average starting model does not result in a substantially better image of the test model. Below 2 m, the Test-Average inverted model is similar to the two-layer models. The similarity of the models inverted with different starting models indicates that the tomography problem is reasonably well behaved and it has found the global minimum.

Again, to assess the reliability of the inversions, Fig. 12 compares the test model, a two-layer starting model, the average of the starting model results, and the standard deviations from the average. The average model images the main features of the test model as well as the other models presented. Not unexpectedly, the standard deviations are greatest above 3 m and at layer boundaries, for example at 6 m depth. Above 3 m, the standard deviations are as large as about 9 m/μs. Below 3 m, the standard deviations are small, less than 1.5 μs/m, indicating that the model is well resolved.

Importance of Reference Model

The reference model is an important parameter for the nonlinear inversion. The second term of the objective function (Eq. 3) is a measure of the misfit between the current model and the reference model, the solution length. The inversion must also minimize this term in conjunction with the data misfit term. The reference model is used to impose some structure on the solution so that reasonable models are found. However, the usual goal of crosshole tomography is to determine the geologic structure between the wells because this information is not well known. The reference model should define the features we are confident exist in the subsurface without including too much detail. To test the effects of imposing structure on the inverted model, I

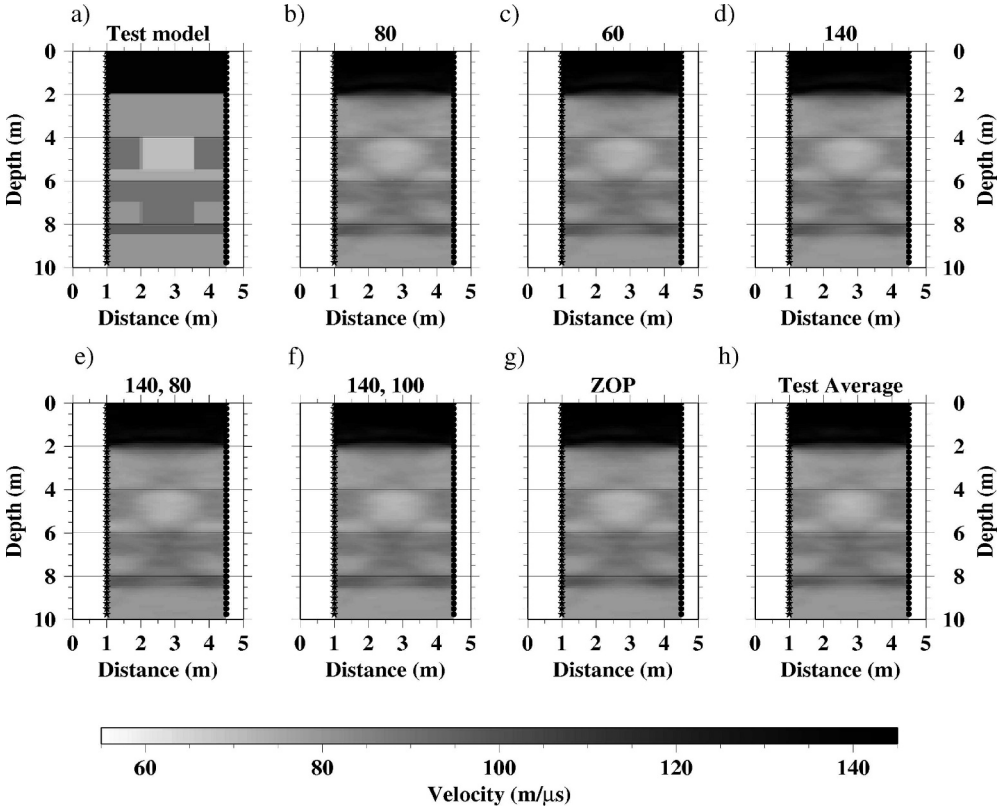

Figure 11. Results of inverting with different the starting models. The plots are arranged in the same order as in Fig. 10 for comparison.

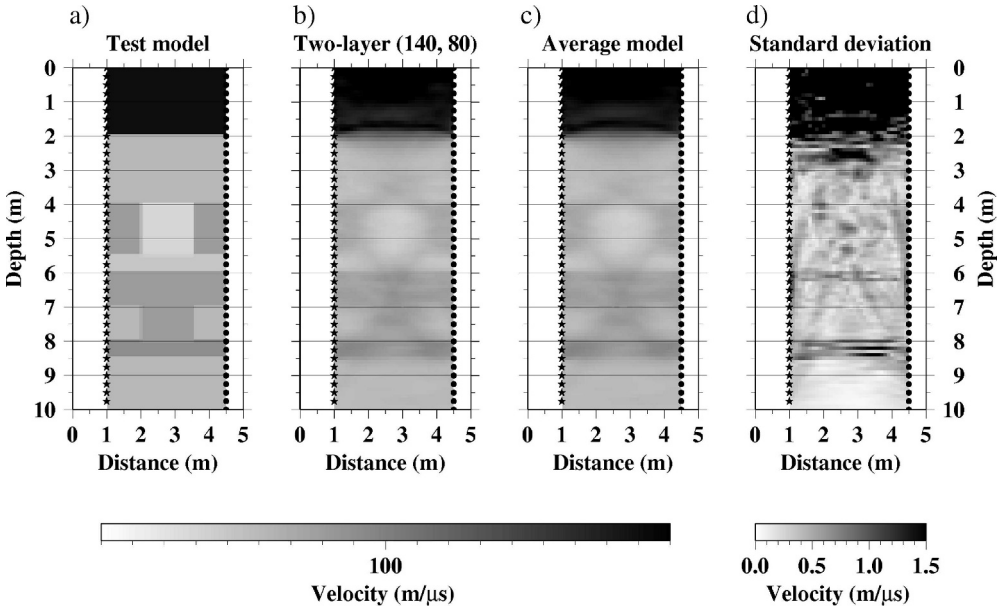

Figure 12. Average starting model and its standard deviations compared to one model and the test model. Standard deviations greater than 1.5 ns are black. The gray scale was chosen to emphasize the small standard deviations below 3 m.

inverted the traveltimes using several different reference models (Fig. 13). These models are the same as the models used in the starting model test (Table 3).

Again, the resulting tomograms are similar (Fig. 14), suggesting that the solution is well behaved. Not surprisingly, the two-layered reference models better image the velocity change at 2 m depth than the constant velocity reference models. This boundary is sharper in the layered reference models, with the exception of the ZOP reference model (Fig. 14g). The ZOP model also contains a thin low velocity zone at about 3 m depth that is not in the other models. As in the starting model test, this layer coincides with the base of the gradient zone in the ZOP starting model. This analysis indicates that simple reference models are sufficient to provide accurate images and that too much structure in the reference model may introduce artifacts.

Figure 15 compares the test model, a two-layer starting model, the average of the reference model results, and the standard deviations from the average. As in the starting model test, the average model images the main features of the test model as well as the other models presented. Again, the standard deviations are greatest above 3 m and at layer boundaries, for example at 6 m depth. At 3 m, a large standard deviation occurs. This depth coincides with the 3 m layer artifact in the ZOP model. The large standard deviations at the layer boundaries, such as 3 m and 6 m, are more distinct than in the starting model test. Another interesting difference is the large change in standard deviation near 6 m depth. In the reference model test, this change is at about 5.75 m whereas in the starting model test, the change is at 6 m. Above 3 m, the standard deviations are as large as about 9 m/μs. Below 3 m, the standard deviations are small, less than 1.5 μs/m, again indicating a well resolved model.

Effect of Grid Size

A difficult decision in parameterizing a tomography problem is choosing the size of the modeling grid cells. I chose four different grid sizes for the comparison: 0.05 m, half the spatial sample interval, 0.1 m, equal to the sample interval, 0.25 m and 0.5 m, both greater than the sample interval. Figure 16 shows the results of this analysis. The inversion routine successfully traced 1640 rays, that is, to all the source-receiver pairs, in the 0.25 and 0.5 m grid size inversion. For the 0.1 m grid size, the inversion traced 1638 rays. However, the inversion for the 0.05 m grid size traced only 1313 rays. Increasing the regularization did little to improve the number of rays traced in the 0.05 m case. The 0.05, 0.1, and 0.25 m grid size image the main features of the test model. The 0.5 m grid size image shows the main features, but they are not as distinct. The 0.05 m grid size model shows an obvious asymmetry in the layering between 7 and 8.5 m. The ray density plot has a higher ray density on the left side of the model than on the right side. This ray density difference probably causes the asymmetry in the velocity model. The ray density asymmetry is less apparent in the 0.1 m grid size inversion. The 0.25 m grid size model shows a velocity gradient from left to right between 2 to 3 m depth. This gradient is more pronounced in the 0.5 m grid size model and extends to 5.5 m depth. All four grid sizes image the main features of the test model

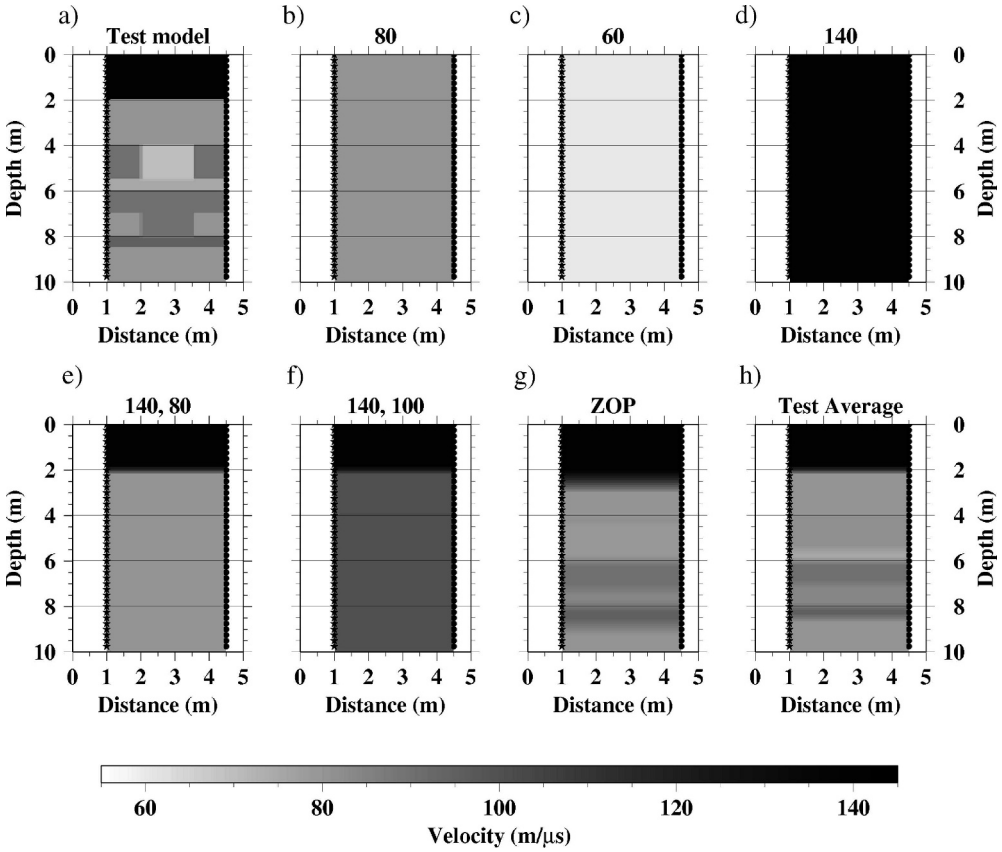

Figure 13. Selected reference models used to assess the dependence of the inversion on the choice of starting model. The test model is shown for comparison.

below 2 m, but the 0.5 m grid size is too large to distinguish the zone boundaries.

Table 4 presents some statistics from the inversions. For the 0.25 m and 0.5 m grid size inversions, the number of iterations was fixed because the RMS residual for later iterations oscillated about the final RMS residual value. The statistics show that the 0.05 m grid size inversion had the lowest RMS residual and the narrowest residual range. However, this inversion only used 1313 traveltimes. The 0.25 m and 0.5 m grid size inversions had small means, but the RMS residual values were greater than the smaller grid sizes and the residual range was greater. An important consideration when choosing the grid size is to ensure that nearly all the traveltimes are used in the inversion. From the grid size analysis, an appropriate grid size would be about the size of the sample interval of the data.

Effect of Ray Coverage

Finally, I study the effects of limited ray coverage on the model. The full traveltime set has rays that encompass angles between approximately −70 and 70 degrees. I windowed the traveltimes for different angular coverages of ±10, ±40, and ±70 degrees. Table 5 lists the statistics from the inversions. Figure 17 shows that using a wide angular coverage better resolves the lateral velocity changes in the model. As the angular coverage narrows, the lateral resolution decreases. In the ±10 degree case, the model consists of horizontal layers with no obvious lateral changes. The ±40 degree case images lateral velocity changes, but the boundaries are more blurred compared to the ±70 case. With near surface tomography acquisition, the distance the energy can propagate limits wide angular coverage, not the geometry of the experiment.

Conclusion

I have presented a synthetic modeling study to examine some of the issues that effect tomographic inversion of crosshole radar data. I looked at the effects of the forward model, the type of model constraints, the starting and reference models, and the grid size. The inversion routines control these factors. I also examined the effect of noise in the data and ray coverage through the model. The field acquisition controls these effects, and once the data has been collected, they can not be changed.

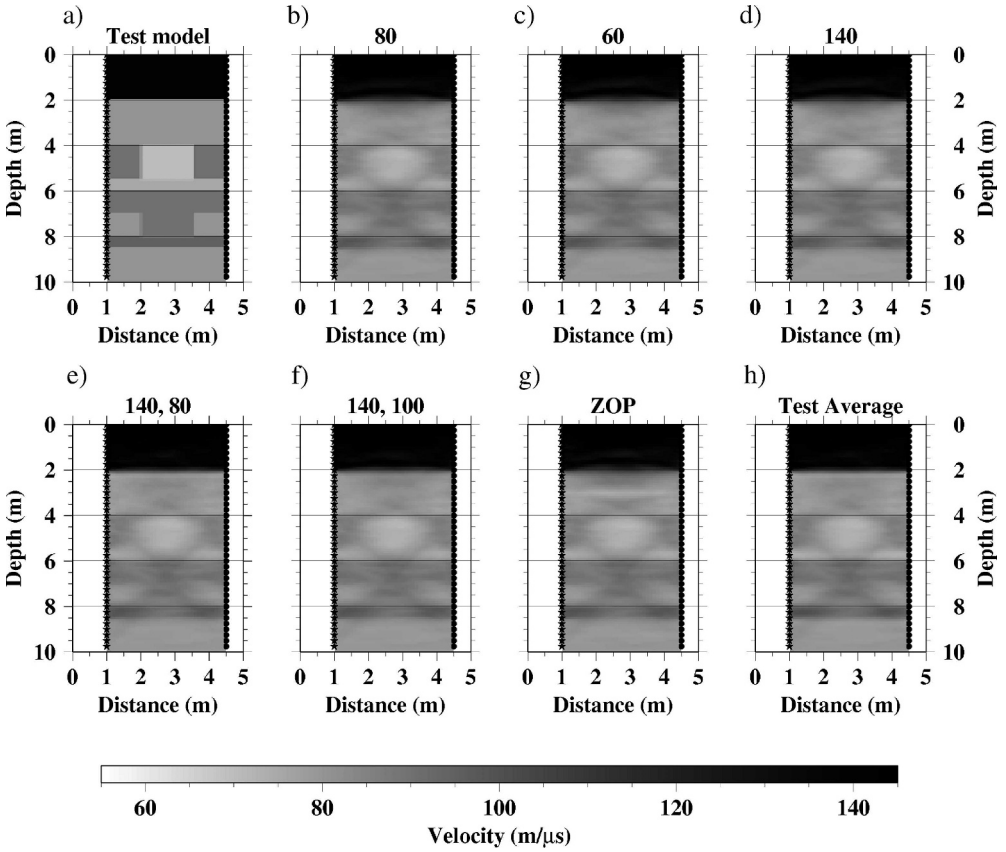

Figure 14. Results of inverting with different the reference models. The plots are arranged in the same order as in Fig. 10 for comparison.

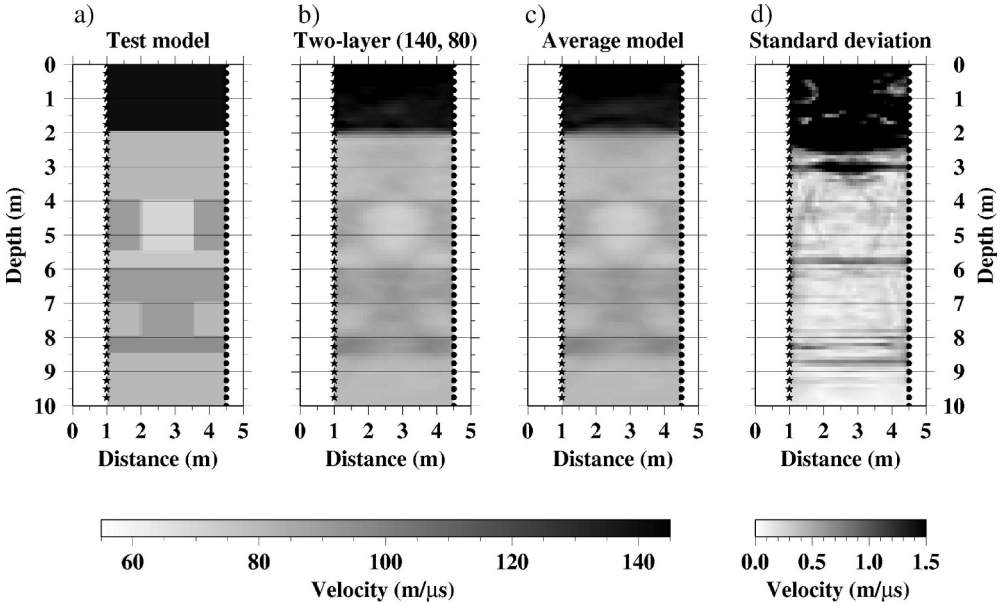

Figure 15. Average reference model and its standard deviations compared to one model and the test model. Standard deviations greater than 1.5 ns are black. The gray scale was chosen to emphasize the small standard deviations below 3 m.

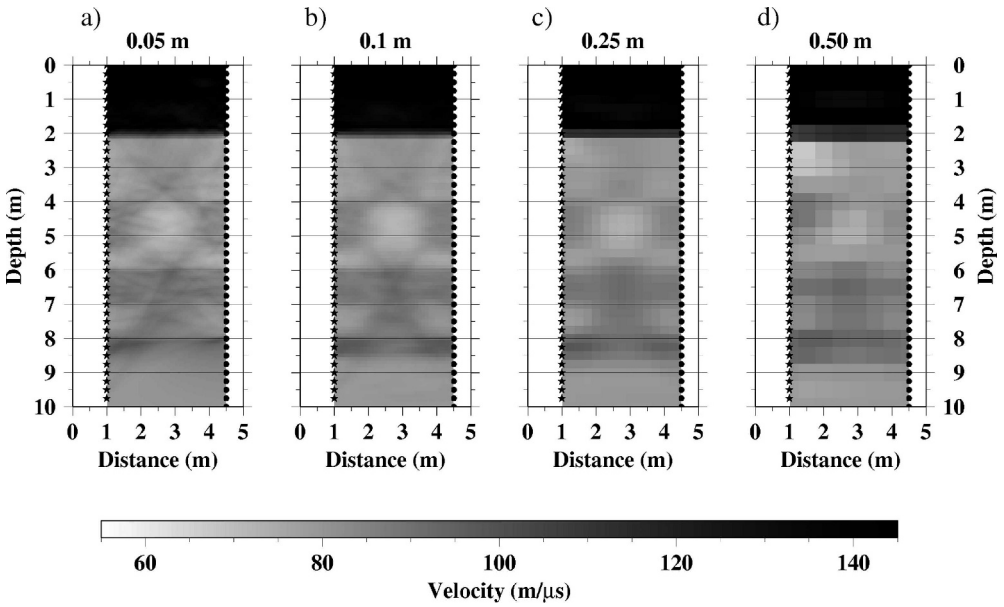

Figure 16. Effects of the grid size used in the forward model and inversion. a) 0.05 m, b) 0.1 m, c) 0.25 m, and d) 0.5 m grids.

The straight ray and curved ray methods imaged the vertical and horizontal velocity changes equally well. However, the reliability of features in the models based on the ray density plots are very different. The straight ray model has the highest ray density at the center of the model and the ray density decreases uniformly away from the center. For the curved ray model, the ray density is heterogeneous with the highest ray densities along velocity boundaries and in a double X-pattern. If ray densities are an indication of model reliability, then the locations of the reliable model features are much different. The curved ray method would provide a better estimate of the reliability since the true ray paths bend between source and receiver.

The greatest effect on the inversion results is the angular coverage of the experiment. Limited aperture experiments will poorly image horizontal velocity variations in the subsurface. The choice of grid size also strongly influences the model. Too small a grid size led to models that did not use all the traveltimes. Too large a grid size resulted in a model that blurred the boundaries of the model and caused velocity artifacts.

Not surprisingly, the amount of noise effects the results. Inverted models from noisy traveltimes did not image the features of the test model reliably and interpretation of those models could lead to misidentification of subsurface features. Noisy traveltimes will poorly image the subsurface. To best image the subsurface, carefully acquiring the data to limit the amount of noise is critical.

However, the type of distribution of the random noise added to the traveltimes had little effect on the results. Even though the objective function is based on a least squares measure of misfit, models from traveltimes with non-Gaussian noise were similar to the Gaussian noise model. The noisy models were also similar to the noise-free model. The distribution of noise appears to have little effect on the resulting model.

Table 4.

Grid size (m)	Mean residual (ns)	RMS residual (ns)	Minimum residual (ns)	Maximum residual (ns)	Iterations
0.05	0.070	0.559	−2.115	2.523	5
0.10	−0.002	0.491	−2.195	2.122	5
0.25	−0.005	0.656	−2.498	2.211	10
0.50	−0.007	1.205	−4.724	4.625	2

Table 5.

Angular coverage	Mean residual (ns)	RMS residual (ns)	Minimum residual (ns)	Maximum residual (ns)	Traced rays
−10, 10	0.019	0.486	−2.903	1.653	196
−40, 40	0.019	0.461	−2.939	1.409	799
−70, 70	0.029	0.460	−3.442	1.982	1636
All	0.032	0.464	−3.442	1.849	1640

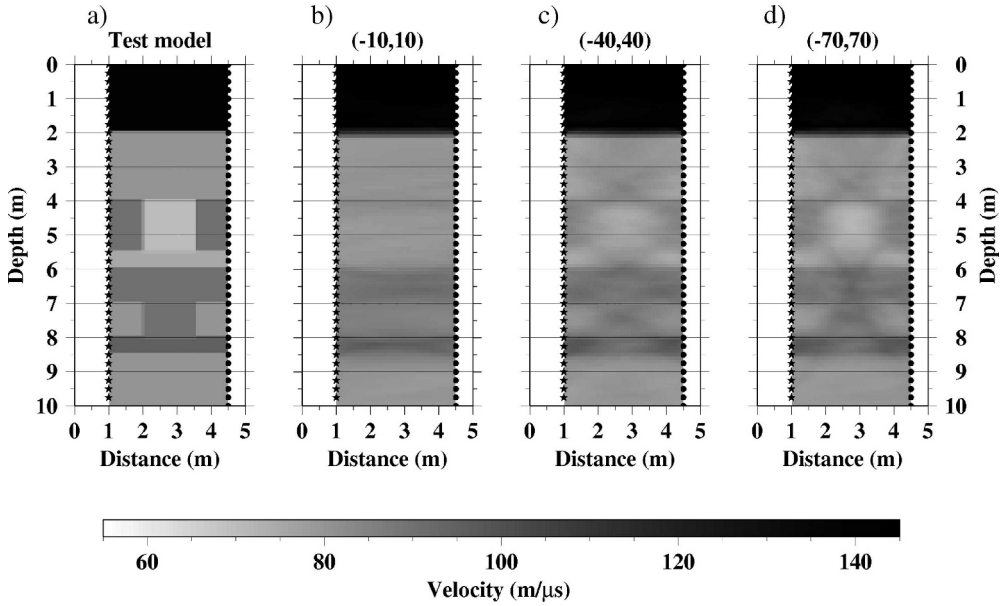

Figure 17. Effects of ray coverage. a) Test model, b) ±10 degrees, c) ±40 degrees, and d) ±70 degrees.

A surprising result of this study is that the starting model, reference model, and type of regularization had little effect on the inverted models. The similarity of the inverted models under different parameterizations indicates that inversions of crosshole tomography are well behaved. By computing the mean and standard deviations of these models, I can appraise their reliability. Below about 2 m, the standard deviations are less than 2 μs/m for different starting and reference models and less than 3 μs/m for the different regularization schemes. The small standard deviations indicate that tomographic models are reliable estimates of the traveltimes.

The most important factor in obtaining reliable results from crosshole tomography is acquiring wide aperture, densely sampled data with little noise. Experiments should be designed to include energy that propagates as close to vertical as possible. Spatial sampling at the size of the expected anomalies or less will provide greater potential to resolve small features in the ground. Fortunately, the choice of starting and reference models and the regularization scheme do not appear to add large artifacts to the models.

Acknowledgments

Inland Northwest Research Alliance grant BSU002 and the U.S. Army Research Office grant DAAD19-00-0454 supported this project. I thank Tom Clemo and Partha Routh for helpful discussions clarifying inverse theory, tomography, and appraisal of the solutions. I thank Marc Buursink for computing the finite-difference waveforms. Contribution no. 0131 of the Center for Geophysical Investigation of the Shallow Subsurface at Boise State University.

References

Aldridge, D.F., and Oldenburg, D.W., 1993, Two-dimensional tomographic inversion with finite-difference traveltimes: Journal of Seismic Exploration, **2**, 257–274.

Alumbaugh, D.L., and Newman, G.A., 2000, Image appraisal for 2-D and 3-D electromagnetic inversion: Geophysics, **65**, 1455–1467.

Alumbaugh, D., Chang, P.Y., Paprocki, L., Brainard, J.R., Glass, R.J., and Rautman, C.A., 2002, Estimating moisture contents in the vadose zone using cross-borehole ground penetrating radar: A study of accuracy and repeatability: Water Resources Research, **38**, 1309, doi:10.1029/2001WR000754.

Barrash, W., and Clemo, T., 2002, Hierarchical geostatistics and multifacies systems: Boise Hydrogeophysical Research Site, Boise, Idaho, Water Resources Research, **38**, 1196, doi:10.1029/2002/WR001436.

Binley, A., Winship, P., Middleton, R., Pokar, M., and West, J., 2001, High-resolution characterization of vadose zone dynamics using cross-borehole radar, Water Resources Research, **37**, 2639–2652.

Chang, P.-Y., Alumbaugh, D., Brainard, J., and Hall, L., 2003, The application of ground penetrating radar attenuation tomography in a vadose zone infiltration experiment, Journal of Contaminant Hydrology, **71**, 67–87.

Clement, W.P., Barrash, W., and Knoll, M.D., 2006, Reflectivity modeling of ground penetrating radar, Geophysics, **71**, K59–K66.

Day-Lewis, F.D., and Lane Jr., J.W., 2004, Assessing the resolution-dependent utility of tomograms for geostatistics, Geophysical Research Letters, **31**, L07503, doi:10.1029/2004GL019617.

Galagedara, L.W., Parkin, G.W., Redman, J.D., and Endres, A.L., 2003, Assessment of soil moisture content measured by borehole GPR and TDR under transient irrigation and drainage, Journal of Environmental and Engineering Geophysics, **8**, 77–86.

Hole, J.A., and Zelt, B.C., 1995, 3-D finite-difference reflection traveltimes, Geophysical Journal International, **121**, 427–434.

Hubbard, S.S., Chen, J., Peterson, J., Majer, E., Williams, K.H., Swift, D.J., Mailloux, B., and Rubin, Y., 2001, Hydrogeological characterization of the South Oyster Bacterial Transport Site using geophysical data, Water Resource Research, **37**, 2431–2456.

Lampe, B., Holliger, K., and Green, A., 2003, A finite-difference time-domain simulation tool for ground-penetrating radar antennas: Geophysics, **68**, 971–987.

Menke, W., 1989, Geophysical data analysis: Discrete inverse theory, Academic Press, Inc., San Diego.

Nolet, G., Montelli, R., and Virieux, J., 1999, Explicit, approximate expressions for the resolution and a posteriori covariance of massive tomographic systems: Geophysical Journal International, **138**, 36–44.

Oldenborger, G.A., Routh, P.S., and Knoll, M.D., 2005, Sensitivity of electrical resistivity tomography data to electrode position errors: Geophysical Journal International, **163**, 1–9.

Paige, C., and Saunders, M., 1982, LSQR: An algorithm for sparse linear equations and sparse least squares: Assn. Comp. Math. Transactions on Mathematical Software, **8**, 43–71.

Peterson, J.E. Jr., Paulsson, B.N.P., and McEvilly, T.V., 1985, Applications of algebraic reconstruction techniques to crosshole seismic data: Geophysics, **50**, 1566–1580.

Podvin, P., and Lecomte, I., 1991, Finite difference computation of travel times in very contrasted velocity models: A massively parallel approach and its associated tools, Geophysical Journal International, **105**, 271–284.

Tronicke, J., Dietrich, P., Wahlig, U., and Appel, E., 2002, Integrating surface georadar and crosshole radar tomography: A validation experiment in braided stream deposits: Geophysics, **67**, 1516–1523.

Tronicke, J., Holliger, K., Barrash, W., and Knoll, M.D., 2004, Multivariate analysis of crosshole georadar velocity and attenuation tomograms for aquifer zonation: Water Resources Research, **40**, W01519, 10.1029/2003WR002031.

Tweeton, D.R., 1988, A tomographic computer program with constraints to improve reconstructions for monitoring in situ mining leachate, U.S. Bureau of Mines, Report of Investigations, RI-9159.

Vidale, J.E., 1990, Finite-difference calculation of travel times in three dimensions: Geophysics, **55**, 521–526.